

Blind calibration of a quantum computer

Liam M. Jeanette,^{1,2,*} Jadwiga Wilkens,³ Ingo Roth,⁴ Anton Than,¹ Alaina M. Green,¹ Dominik Hangleiter,^{5,6,†} and Norbert M. Linke^{2,1}

¹*Joint Quantum Institute, University of Maryland, College Park, MD 20742, USA*

²*Duke Quantum Center, Duke University, Durham, NC 27701, USA*

³*Institute for Integrated Circuits, Johannes Kepler University Linz, 4040 Linz, Austria*

⁴*Quantum Research Center, Technology Innovation Institute, Abu Dhabi, UAE*

⁵*Simons Institute for the Theory of Computing, University of California at Berkeley, Berkeley, CA 94720, USA*

⁶*Joint Center for Quantum Information and Computer Science, NIST/University of Maryland, College Park, MD 20742, USA*

(Dated: January 10, 2025)

Quantum system calibration is limited by the ability to characterize a quantum state under unknown device errors. We develop an accurate calibration protocol that is blind to the precise preparation of a specific quantum state. It extracts device errors from simple tomographic data only, and does not require bespoke experiments for a priori specified error mechanisms. Using a trapped-ion quantum computer, we experimentally demonstrate the accuracy of the method by recovering intentional miscalibrations. We then use blind calibration to estimate the native calibration parameters of the experimental system. The recovered calibrations are close to directly measured values and perform similarly in predicting state properties.

I. INTRODUCTION

In order to build and calibrate large-scale, low-noise quantum computers, precise and accurate characterization techniques are needed, which are also data-economical and light on post-processing. Quantum state tomography [1, 2], detector tomography [3, 4] and process tomography [5, 6] are all designed to achieve this for different aspects of a quantum computing device. They are limited by the quality of their input data, which are generally only as precise and accurate as the measurement apparatus itself, a problem known as the *calibration problem* [7]. At least a single high-quality component of an experiment, say high-quality measurement [7] or state preparation [8, 9], seems to be required in order to serve as a reliable probe to characterize the system in a set of independent calibration measurements.

This is why it is desirable to solve the calibration problem in a different way. Consider the example of super-resolution spectroscopy techniques [10, 11], where a fundamental limit—the Nyquist limit—is overcome by making an assumption about the signal, for instance, that it is composed of a single or few frequency components. Then, only a very small number of measurements is required to obtain a highly precise estimate of the frequency of a signal.

Similarly, structural properties of the signal, which are known a priori, can be used to solve the calibration problem on a quantum computer and distinguish different types of errors in an experimental setup, see Fig. 1(a). A prominent example of such a solution for calibration is gate set tomography [12–15], where the measurements generated by a gate set are exploited in order to self-consistently perform tomography of the gate set even in the presence of state preparation and measurement (SPAM) errors. Recently, a number of techniques have been proposed to characterize SPAM errors in order to

then accurately calibrate a quantum computing device—a task that has been referred to as ‘self-calibrating’ [16–20], ‘self-consistent’ [21], ‘simultaneous’ [22], or ‘blind’ [23] tomography. Other protocols solve the state tomography problem in a way that mitigates measurement errors [24, 25], or model measurement errors in order to obtain more precise estimates of quantum instruments [26].

Here, we experimentally demonstrate that the calibration parameters of a small ion-trap quantum computer can be extracted from simple projective Pauli measurement data in a way that is blind to the precise state preparation. Our blind calibration technique does not require independently characterized calibration devices or experiments, and achieves calibration accuracies similar to traditional direct measurements. We make use of the blind tomography protocol introduced in Ref. [23]. Our method is able to recover many different calibration parameters as well as a tomographic state estimate.

We use blind calibration to characterize single-qubit over-rotation, nearest- and next-nearest-neighbour crosstalk, classical readout and detector spillover errors on the trapped-ion quantum computer. We numerically benchmark blind calibration for the same setting, and show an inverse square-root scaling of both the error on the recovered calibration and states with the number of measurements. Then, we experimentally verify the method by accurately recovering intentional miscalibrations. Finally, we optimize the sensitivity of our method to calibration errors, and its robustness to state-preparation errors over different probe states. The calibration parameters extracted using the optimal probe states are of similar accuracy as those extracted in independent experiments for readout errors and crosstalk.

II. BLIND CALIBRATION

For blind calibration, we consider measurement data

$$y_i(\zeta, \rho) = \text{tr}[M_i(\zeta)\rho], \quad (1)$$

* liam.jeanette@duke.edu

† mail@dhangleiter.eu

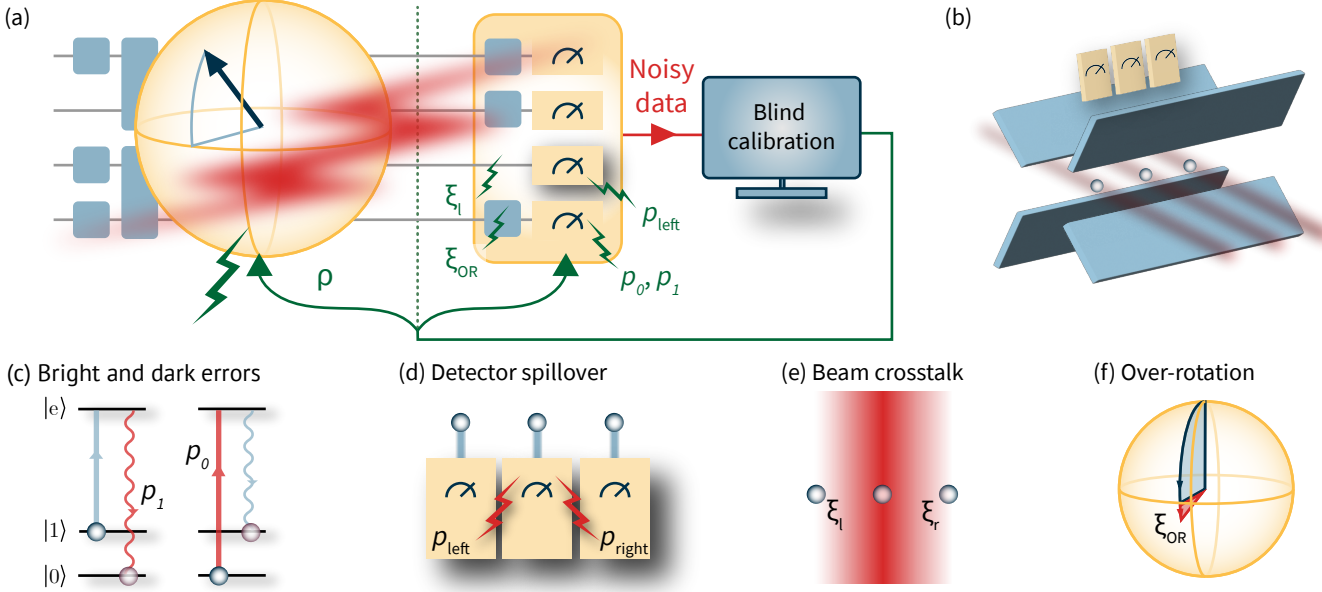


FIG. 1. **Blind calibration of a trapped ion quantum computer.** (a) Since errors happen throughout a quantum computation, it is difficult to distinguish measurement errors from state preparation errors. The blind calibration protocol uses prior knowledge about the structure of the data in order to distinguish those errors in noisy data and thus allows us to accurately calibrate the device. (b) Experimental setup. Ions are held in a linear Paul trap, probed using individual laser beams, and detected using individual detector channels. (c) Ion fluorescence on the transition between the computational state $|1\rangle$ and an excited state $|e\rangle$ is used for readout. A bright error occurs when an ion in the bright $|1\rangle$ state off-resonantly decays to the dark $|0\rangle$ state with probability p_1 or vice versa a dark error with probability p_0 . (d) In a detector spillover error, a signal on one detector generates spurious photon counts on adjacent detectors due to electrical or optical crosstalk. This causes a false detection on the left detector with probability p_{left} , and on the right detector with probability p_{right} . (e) A crosstalk error occurs, when the laser beam targeting a particular ion causes unintended rotation by an angle $\xi_r (\xi_l) \cdot \frac{\pi}{2}$ on the neighboring right (left) ion. (f) A target $\frac{\pi}{2}$ operation over- or under-rotates by an angle $\xi_{\text{OR}} \cdot \frac{\pi}{2}$.

obtained from measurements on an unknown quantum state ρ of Hermitian operators $M_i(\zeta)$, where $i = 1, \dots, m$, that depend, potentially non-linearly, on calibration parameters $\zeta \in \mathbb{R}^k$. The blind tomography task, introduced by Roth *et al.* [23], is to simultaneously infer ρ and ζ from the data vector $y \in \mathbb{R}^m$. In blind calibration, we use blind tomography as developed in Ref. [23] on noisy state preparations ρ_i in order to obtain an estimate of the device calibration ζ .

Consider a tomographically complete set of measurement operators \mathcal{O} . In the miscalibrated scenario, instead of $M \in \mathcal{O}$ we thus effectively measure an operator $M(\zeta) = \sum_{M' \in \mathcal{O}} \xi_{M \rightarrow M'}(\zeta) M'$. Here, the $\xi_{M \rightarrow M'}(\zeta)$ are linear coefficients obtained when decomposing $M(\zeta)$ into the tomographically complete set \mathcal{O} . We can now group terms with the same $\xi_{M_i \rightarrow M'}(\zeta) =: \xi_j(\zeta)$ into operators $N_{i,j}$, and rephrase the blind tomography model as a linear sum

$$y_i(\zeta, \rho) = \sum_j \xi_j(\zeta) \text{tr}[N_{i,j} \rho] \equiv \mathcal{A}(\xi, \rho)_i. \quad (2)$$

Linearizing the dependence on ζ we can always reduce the number of calibration coefficients ξ_j to at most $k + 1$ linearly independent coefficients. We set $N_{i,0} = M_i$ to be the ideal target measurement. Thus, when the device is already perfectly calibrated, the linear coefficients are $\xi_0 = 1$ and $\xi_j = 0$ for all $j > 0$.

There are two cases of particular interest. The first case is a coherent error, when $M(\zeta) = e^{-i\zeta G/2} M e^{i\zeta G/2}$ for some

rotation generator G . If M, G are anti-commuting Pauli operators we find $M(\zeta) = \cos(\zeta)M + i \sin(\zeta)MG$, so that $\xi_{M \rightarrow M} = \cos(\zeta)$ and $\xi_{M \rightarrow iMG} = \sin(\zeta)$, which we can linearize as $M(\zeta) \approx M + i\zeta MG$ for small errors. The second case is an incoherent readout error, which we model as a stochastic matrix S acting on the computational-basis measurement outcomes $b \in \{0, 1\}^n$, $|b\rangle\langle b| \mapsto \sum_{c \in \{0, 1\}^n} S_{bc} |c\rangle\langle c|$. If a measurement is performed in a basis different from the computational basis, the states $|c\rangle$ should be understood as the ± 1 -eigenstates $|b\rangle_M$ of the corresponding measurement operator M .

In order to further improve the precision of blind calibration, we use projective measurements $M_i = M_i^2$ rather than Pauli expectation-value estimates as done in Ref. [23]. Projective measurements in all 3^n Pauli bases (with 2^n possible outcomes each) describe the natively available measurement data and contain more information than expectation-value measurements of Pauli observables in the finite-sample regime. The two models can be translated into one another using the relation $|b\rangle\langle b|_M = (1 + (-1)^b M)/2$, where M is a Pauli matrix and $b \in \{0, 1\}$. In Appendix A, we demonstrate the improvement in the precision of the recoveries.

In Ref. [23], it was proven that the blind tomography problem can be solved in principle assuming that the state preparation is approximately pure, and that only a small number of calibration errors actually affect the data. To solve the blind

tomography problem in practice, we minimize the bilinear objective function

$$f(\xi, \rho) = \frac{1}{2} \|\hat{y} - \mathcal{A}(\xi, \rho)\|_{\ell_2}^2 \quad (3)$$

over quantum states ρ and calibration vectors ξ using an alternating gradient descent (AGD) or block-coordinate descent optimization. Here, \hat{y} is the experimentally measured data and $\|\cdot\|_{\ell_2}$ denotes the Euclidean norm. Importantly, our approach enforces that ρ is a valid pure quantum state, and the entries of ξ take only allowed values, for example, values between 0 and 1 for calibration parameters that are probabilities. These structural assumptions about the data allow us to distinguish different sources of error and thus to solve the blind calibration problem. The idea of AGD minimization is to alternate gradient steps with respect to $f(\rho, \xi)$ over ρ , while fixing $\xi = \xi_k$, and over ξ while fixing $\rho = \rho_k$ to the most recent results of a gradient step, ξ_k and ρ_k , respectively. We perform Riemannian gradient descent with respect to the manifold of pure quantum states [23] and Euclidean gradient-descent for the calibration vectors, respectively, and post-project onto the set of valid assignments after a gradient step.

III. EXPERIMENTAL SETUP AND CALIBRATION ERRORS

We use a trapped-ion quantum computer consisting of a linear chain of $^{171}\text{Yb}^+$ ions trapped in a linear Paul trap as shown in Fig. 1(b). Qubit states $|0\rangle$ and $|1\rangle$ are encoded in the hyperfine states of the ground level, $|^2S_{1/2}, F = 0, m_F = 0\rangle$ and $|^2S_{1/2}, F = 1, m_F = 0\rangle$, respectively. Each qubit is initialized to $|0\rangle$ using optical pumping [27], and coherent operations are applied to prepare an arbitrary state using individually addressed Raman beams [28]. The state of each ion can be read out individually in the qubit Z -basis using state-dependent fluorescence, in which ions in the $|1\rangle$ state emit photons that are counted with a multi-channel photomultiplier tube (PMT), and ions in $|0\rangle$ remain dark.

For blind calibration, we perform projective measurements in all Pauli bases. In order to implement those measurements, we apply $\pi/2$ -single-qubit rotations around the X or Y axis, $R_X(-\frac{\pi}{2})$ or $R_Y(\frac{\pi}{2})$, respectively, before the native measurement in the computational Z -basis. We then model the dominant sources of measurement errors in the trapped-ion system and calculate the corresponding transformations of each Pauli basis. Finally, we combine individual errors to construct the measurement map \mathcal{A} according Eq. (2).

a. Over-rotation When applying single-qubit basis rotations, $R_X(\frac{\pi}{2})$ and $R_Y(-\frac{\pi}{2})$, there is a possibility of over- or under-rotating the qubit by an angle of $\pm\xi_{\text{OR}} \cdot \pi/2$, shown in Fig. 1(f). Assuming the angle of this excess rotation is small, it results in an unwanted projection into the Z basis, leading to transformed Pauli observables

$$X \mapsto X - \xi_{\text{OR}}\pi Z \quad (4)$$

$$Y \mapsto Y - \xi_{\text{OR}}\pi Z. \quad (5)$$

Since no single-qubit rotations are performed to measure in the native Z basis, only the X and Y bases are affected by over-rotation errors.

b. Dark and bright errors To perform state readout, we excite a cycling transition from $^2S_{1/2}(F = 1) \rightarrow ^2P_{1/2}(F = 0)$. Ions in $|1\rangle$ fluoresce, while ions in $|0\rangle$ remain dark. During this process, the laser can off-resonantly drive a transition that causes decay into the opposite state with probability, where it can be incorrectly measured. We call this *dark error* or *bright error*, occurring with probabilities p_0 and p_1 , respectively, as shown in Fig. 1(c). Under a dark error, the $|0\rangle$ -state projector transforms as

$$|0\rangle\langle 0|_M \mapsto (1 - p_0)|0\rangle\langle 0|_M + p_0|1\rangle\langle 1|_M \quad (6)$$

in all Pauli bases $|b\rangle_M$.

c. Detector spillover During the fluorescence detection process, photons emitted by individual ions are collected and counted on individual channels of a detector array. After a fixed detection time, a threshold for the photon number is used to discriminate ions in state $|0\rangle$ and state $|1\rangle$. Due to imperfect alignment of the detector and electrical crosstalk between the channels, photon counts from a bright ion may spill over to neighboring channels as shown in Fig. 1(d), potentially resulting in a dark ion being classified as bright.

Detector spillover errors occur with probabilities p_{left} to the left and p_{right} to the right. Unlike the previous errors, detector spillover is a purely multi-qubit error. Right detector spillover transforms basis states as

$$|10\rangle\langle 10|_M \mapsto (1 - p_{\text{right}})|10\rangle\langle 10| + p_{\text{right}}|11\rangle\langle 11|. \quad (7)$$

d. Beam Crosstalk During single-qubit rotations on a target ion, light from the laser beam may cause unwanted illumination of neighboring ions as shown in Fig. 1(e) causing a rotation by some angle $\xi_l \cdot \pi/2$ on the left ion and $\xi_r \cdot \pi/2$ on the right ion. Such crosstalk also introduces unintended phase differences ϕ_l and ϕ_r between the target qubit and its left and right neighbours.

Unlike the previous errors, beam crosstalk transformations do not have a simple form. Instead, we must determine the unitary that acts on the qubits as a result of both the applied gates on the target qubits as well as the induced rotations on the neighboring qubits. With this unitary, we calculate the overall transformation on the Pauli bases. For example, to measure the Pauli string XY on two qubits, we apply an $R_Y(\frac{\pi}{2})$ gate to qubit 1 and an $R_X(\frac{\pi}{2})$ gate to qubit 2. Considering the crosstalk from these two gates, we get the resulting transformed Pauli to first order in ξ_l, ξ_r as

$$XY \mapsto XY + \xi_l \pi \cos(\phi_l) YY + \xi_l \pi \sin(\phi_l) ZY - \xi_r \pi \sin(\phi_r) XZ. \quad (8)$$

The four independent calibration parameters we recover are then $\xi_l \cos(\phi_l)$, $\xi_l \sin(\phi_l)$, $\xi_r \cos(\phi_r)$, and $\xi_r \sin(\phi_r)$.

e. Combining Errors To construct the final measurement map \mathcal{A} , the transformations due to individual errors on individual or pairs of qubits must be combined. This will lead to higher-order effects, which we neglect, keeping only terms that are linear in the calibration parameters $p_0, p_1, p_{\text{left}}, p_{\text{right}}, \xi_{\text{OR}}, \xi_l$, and ξ_r .

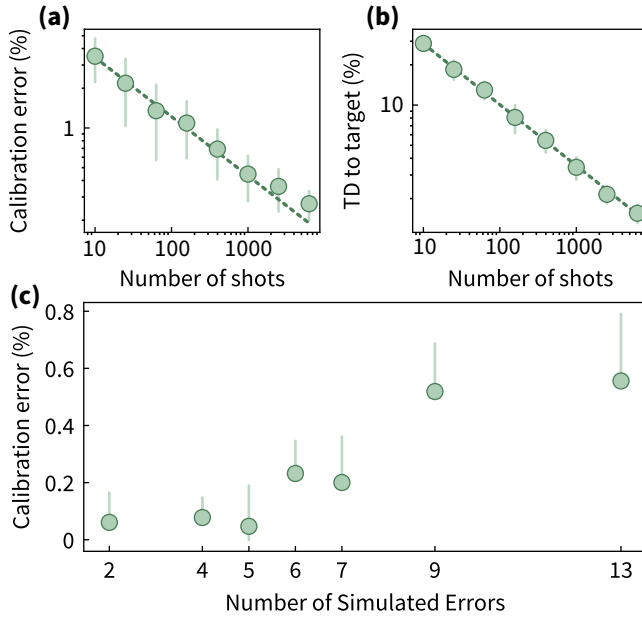


FIG. 2. Numerical benchmarks of blind calibration using a noiseless three-qubit GHZ state and the four error types with nine calibration parameters discussed in the main text, with parameters set to values ξ_{actual} given in Eq. (C13) of Appendix C. (a) Calibration error for the nine recovered parameters. The recovered parameters are used to perform calibrated state tomography, with the resulting trace distances to the target shown in (b). Both calibration error and trace distance are shown as a function of the number of experimental shots per basis (circles) with one standard deviation error bars, decaying as an inverse square root (dashed line). (c) Calibration parameter recovery with increasing number of errors from dark and bright errors (2 parameters), detector spillover errors (2), over-rotation error (1), symmetric beam crosstalk (1), asymmetric beam crosstalk (1), asymmetric beam crosstalk with phase (2), and next-nearest-neighbor asymmetric crosstalk with phase (4).

IV. RESULTS

A. Numerical benchmarks

To benchmark the blind calibration procedure, we numerically simulate quantum circuits with miscalibrations. Specifically, we use a noiseless three-qubit GHZ-state, and simulate miscalibrated projective measurements. We measure the quality of the recovered calibrations in the *calibration error*

$$E(\xi, \tau) := \frac{1}{k} \sum_{j=1}^k |\xi_j - \tau_j|, \quad (9)$$

measured by the normalized ℓ_1 -norm between the recovered calibration parameters ξ and the true parameters τ .

In order to assess the quality of the calibration parameters inferred from blind calibration when the true parameters are unknown, we perform state tomography on the same type of experimental data in a way that is informed by the estimate of the calibration parameters, see Appendix B for details. We then compute the trace distance (TD) of the state estimate ρ to

the target state ψ ,

$$d_{\text{tr}}(\rho, \psi) = \frac{1}{2} \text{tr}(|\rho - \psi|), \quad (10)$$

as a figure of merit for the quality of the calibration, in place of the *unknown* distance to the experimentally prepared state. We expect this to be a good figure of merit, as we do not expect miscalibrations to conspire to yield tomographic estimates that are closer to the target state compared to the perfectly calibrated scenario.

Fig. 2(a-b) shows the performance of blind calibration using simulated data in terms of the calibration error and TD to the target state. Because there are no state preparation errors, any deviation from the target state is due to shot noise and calibration errors. As we increase the number of simulated shots, decreasing the statistical uncertainty, we see that the deviation from the target state and expected errors both tend toward the expected result following an inverse square root decay. This shows that the miscalibrations are recovered to sufficient accuracy so that they do not limit the state recovery. We are able to recover calibration errors to well within 1% using only 1000 shots per measurement basis.

There is a trade-off between the number of error mechanisms included in the calibration model and the precision with which they can be recovered. As we increase the number of calibration parameters, it becomes harder to distinguish different errors, leading to an increased error. We observe this effect in Fig. 2(c), which shows that the calibration error for the nine calibration parameters we consider in this work remains reasonably small.

B. Experimental results

We first verify the error recovery by intentionally miscalibrating our experimental system. We prepare a three-qubit random product state and add varying amounts of over-rotation and beam crosstalk errors to the system. For over-rotation errors, we add a small extra angle to the target qubit, while for beam crosstalk errors, we add small rotations to the neighboring qubits. We add rotations of 0%, 1%, 2.5%, and 5% (of $\frac{\pi}{2}$) and correct the data for classical readout errors (see Appendix D 1 a) to ensure only rotational measurement errors are present. We then use blind calibration to recover the injected errors, shown in Fig. 3(a). We find accurate recoveries of the injected miscalibrations.

To assess the quality of the blind calibration estimates, we perform *standard tomography*, where the calibration is assumed to be perfect (i.e. $\xi = 0$), *direct-calibration tomography*, where the calibration parameters are those obtained from direct measurements on the device or prior knowledge, and *blind-calibration tomography*, where we use the parameters obtained in blind calibration. The results for the intentionally miscalibrated setup are shown in Fig. 3(b-d), respectively. They demonstrate that, as expected, the quality of standard tomography (b) decreases with the amount of miscalibration. In contrast, when using the directly measured (i.e., in this case,

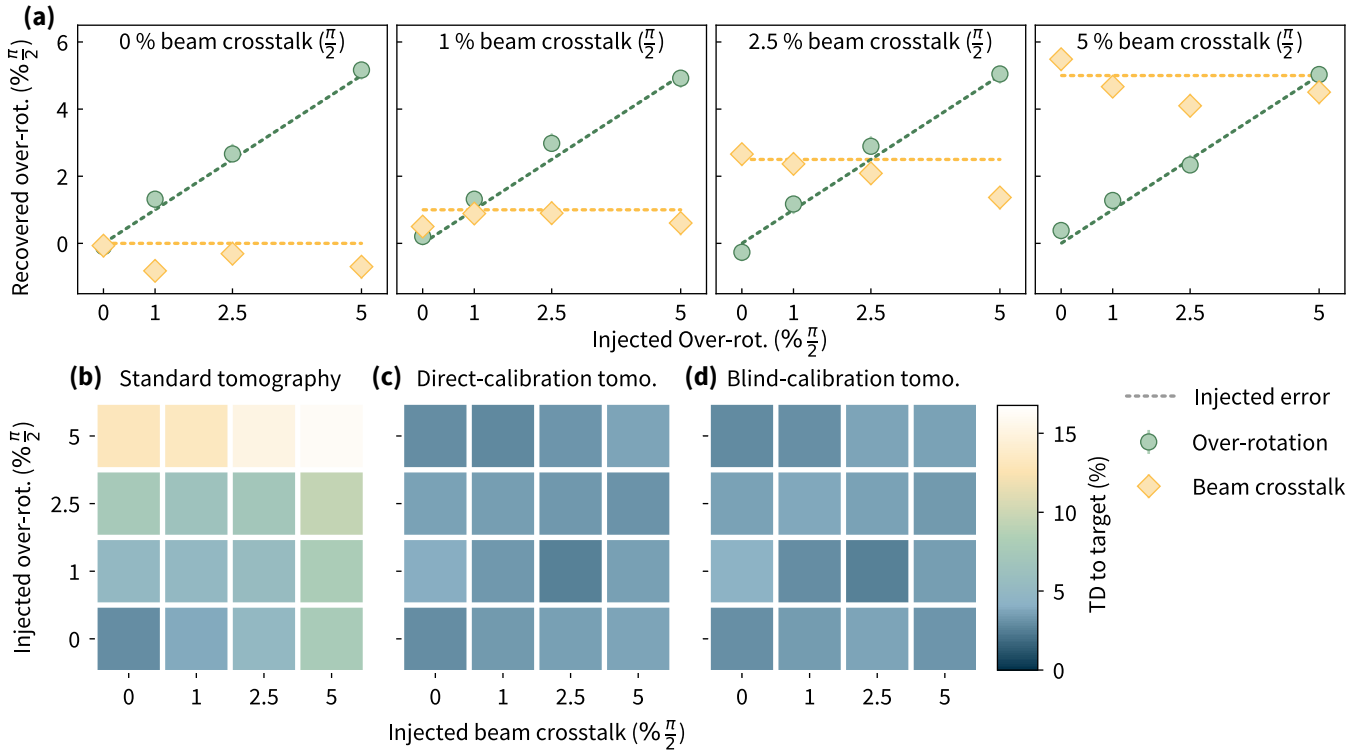


FIG. 3. Recovery of intentional miscalibrations. In order to demonstrate the experimental viability of blind calibration, we intentionally inject over-rotation and nearest-neighbour beam crosstalk errors (with $\xi_r = \xi_l$) of varying magnitude $[0, 1, 2.5, 5] \cdot \% \frac{\pi}{2}$ by performing appropriate single-qubit rotations, when taking tomographic data of a randomly drawn 3-qubit product state in the X - Z plane with polar angles given by $\theta_1 = 1.237\pi, \theta_2 = 0.670\pi, \theta_3 = 1.823\pi$. (a) Blind-calibration estimates of the over-rotation (green circles) and crosstalk errors (yellow diamonds) compared to the injected errors (green/yellow dashed lines) as a function of the injected over-rotation for different values of injected beam crosstalk. (b) Assessment of the quality of different calibrations using the trace distance (TD) to the target state of the state estimate obtained from standard tomography, direct-calibration tomography, and blind-calibration tomography.

the injected) calibration parameters (c) and the parameters obtained from blind calibration (d) to inform tomography, we find that the quality of the state recovery remains constant independent of the amount of miscalibration. Blind calibration also matches the performance of the direct calibrations in terms of the TD to the target state.

In our last set of experiments, we aim to identify the native errors in the system. These are smaller and hence require higher-precision estimates than the injected errors. We observe that different states vary in their sensitivities to the errors present in the system. To perform our calibration with high precision and robustness to state preparation errors, we find a set of product states that provide optimal recoveries for the expected set of errors with simulated data, see Appendix D2 for details. We prepare these states and perform blind calibration to obtain a set of optimal calibration recoveries. The resulting calibration parameters for two readout errors and two rotation errors are shown in Fig. 4 (a) and (b), respectively. The full set of estimated calibration parameters is shown in Appendix D3. The estimated parameters show close agreement with the best estimates from direct experimental diagnostics, where available, as discussed in Appendix D1, see also Fig. 4(c). To assess the quality of the parameters obtained from blind calibration in comparison to the direct ex-

perimental diagnostics we again turn to the trace distance to the target state of the tomographic estimate using the respective calibrations, see Fig. 4(d). We compare the quality of the calibrations obtained from blind tomography on the optimal probe states with the those obtained from direct experimental diagnostics for the recovery of various state preparations in Fig. 4(e). We find that the calibration parameters from blind calibration yield state estimates closer to the target than uncalibrated standard tomography. This shows that the parameters obtained from blind calibration generalize to independent experiments on different states and thus are not an artifact of overfitting. They also perform similarly well compared to the calibration parameters obtained from direct diagnostics, demonstrating the efficacy of blind calibration.

V. DISCUSSION AND OUTLOOK

In this work, we develop a method to calibrate a quantum computer that is blind to the specific state preparation and its accuracy, and thus provides a solution to the calibration problem [7]. Blind calibration requires tomographic data only and thus offers an easy-to-use and data-efficient method for calibrating quantum computing systems that fundamentally cir-

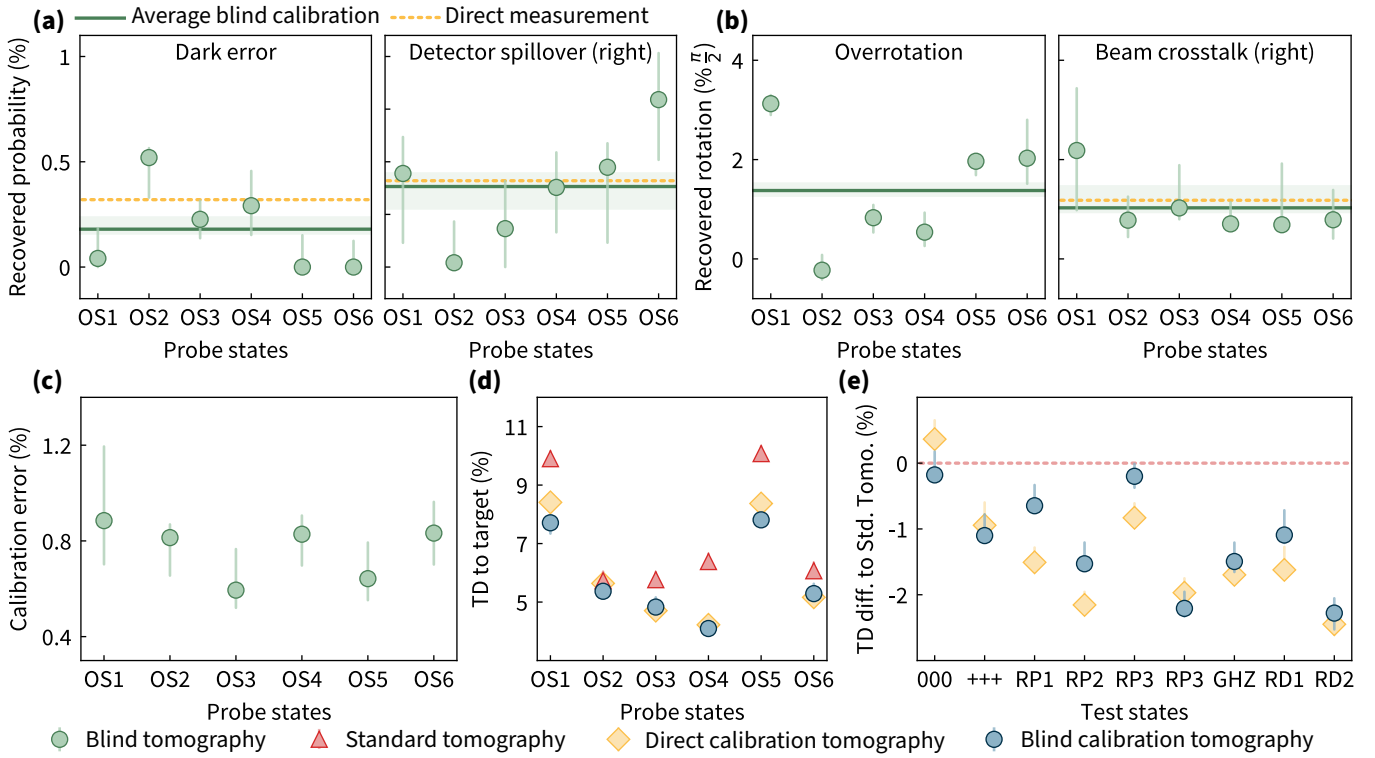


FIG. 4. **Blind calibration of the native errors of the trapped-ion quantum computer** using six optimal *probe states* labeled OS1 to OS6, see Appendix D 2 for details. Blind-calibration estimates of the calibration parameters are represented by green circles with one standard deviation error bars. The average of the estimated calibration parameters over the six probe states and its standard deviation are represented by a solid green line and shaded area, respectively, and the estimates from the direct measurement by dashed yellow lines. (a) Estimates of dark error p_0 and right detector spillover error p_{right} . (b) Estimates of over-rotation ξ_{OR} and right beam crosstalk ξ_r . (c) Calibration error $E(\xi, \delta)$ of the blind calibration (ξ) compared to direct measurements (δ). (d,e) To assess the quality of different calibrations, we compute the distance (TD) to the target state of the state estimates obtained from standard tomography (triangles), direct-calibration tomography (diamonds), and blind-calibration tomography (circles). For blind-calibration tomography, we use the averages obtained from the six optimal probe states as our calibration parameter estimates. In (d), we show the quality of the estimates for tomographic data from the six probe states OS1–OS6. (e) To demonstrate that the blind calibration generalizes beyond the probe states, we also obtain tomographic data from several independent *test states*: the basis state $|000\rangle$, the Hadamard basis state $|+++ \rangle$, four random product states labeled RP1 to RP4, the GHZ state, and two states generated by random deep circuits, labeled RD1 and RD2, see Appendix D 2 for details. We show the difference $d_{\text{tr}}(\rho^*, \psi) - d_{\text{tr}}(\rho, \psi)$ of the trace distances between the standard tomography estimate ρ and the direct/blind calibration estimate ρ^* to the target state ψ . In this representation, standard tomography achieves a value of 0 (solid line), and the more negative the values of direct/blind-calibration tomography are, the closer the corresponding state estimate is to the target state.

cumvents many of the problems of traditional direct calibration methods. Importantly, a single set of experimental data is sufficient to characterize many calibration errors of different type rather than requiring tailored measurements for each individual error as is the case of traditional direct techniques.

Another important advantage of blind calibration is that since the same set of experimental data is used for all calibrations, calibration can be done *post hoc* in a “measure-first-think-later” mindset similar to classical shadows [29–31]. If an experimenter is unsure about the dominant sources of error affecting their system, they can simply take a set of tomographic data and then compare how well different error models describe the data in post-processing. In fact, when we performed blind calibration of the native device errors (Fig. 4), only after analyzing the experimental data did we realize that different calibration parameters are required to ac-

count for beam crosstalk errors. A systematic way to do this was sketched in Ref. [23], using sparse recovery techniques.

Our calibration experiments use data from three qubits, which is enough to calibrate measurement errors with at most next-nearest-neighbor interactions, assuming consistent errors across qubits. When the number of dominant errors in a system is large, larger probe states may be required. However, a larger number of qubits may also introduce additional independent calibration parameters, giving rise to a trade-off.

When modeling the errors in the ion-trap system, we assume small errors, allowing us to approximate them to first order in the calibration parameters ξ . This introduces approximation errors on the order of ξ^2 . In our setting, this is a valid approximation since large errors are easily isolated and characterized by direct experimental diagnostics, e.g., Rabi flopping on non-addressed ions, see also Appendix D 1. For more

precise calibration and for large calibration errors, it may be necessary to model the errors affecting the system exactly. Our solution to the blind calibration problem using alternating minimization is able to account for such nonlinear terms, but finding the optimal solution may be more challenging.

Further increases in accuracy could be achieved by running a ‘hybrid scheme’ wherein some calibration parameters that are known a priori with high precision are fixed, while others are found using blind calibration.

Blind calibration is a general framework and can be applied to any physical platform and its specific error profile. Future work should establish the limits to the number and types of calibration errors that can be simultaneously recovered.

To maximize accuracy we perform optimization over different probe states. We limit this optimization to product states since those states can be prepared with highest fidelity, and in order to restrict the optimization space. An intriguing problem that we leave open is to develop a detailed theory of sensitivity for blind calibration. Identifying properties of good probe states for certain error models would allow us to cheaply identify suitable states sensitive to those errors as the probe system is scaled up.

ACKNOWLEDGMENTS

This material is based upon work supported by the U.S. Department of Energy, Office of Science, National Quantum Information Science Research Centers, Quantum Systems Accelerator (DE-FOA-0002253). Additional support is acknowledged from the National Science Foundation, Quantum Leap Challenge Institute for Robust Quantum Simulation (OMA-2120757) and Software-Tailored Architecture for Quantum Co-Design (STAQ) Award (PHY-2325080). DH is grateful for support from the Simons Institute of the Theory of Computing, supported by DOE QSA. JW has been supported by the project High-Performance Integrated Quantum Computing (FFG 897481) within Quantum Austria. The authors thank Yingyue Zhu for support with the experiments, and Michael Straus and Nhung Nguyen for helpful discussions.

APPENDICES

A. Blind calibration algorithm	7
B. Calibrated state tomography	8
C. Error models	9
D. Native system calibration	10
1. Direct measurements	10
a. SPAM	10
b. Beam crosstalk	10
2. Blind calibration	10
a. Optimal states	12
b. Test states	12
3. Full recovery	12

References	12
------------	----

Appendix A: Blind calibration algorithm

This section describes the alternating gradient descent (AGD) optimization algorithm for solving bilinear calibration problems over quantum states ρ and calibration vectors ξ . The algorithm minimizes Eq. (3) via an iterative procedure based on gradient descents on Riemannian manifolds. Each iteration alternates between a gradient step with respect to ρ for fixed ξ and a gradient step with respect to ξ for ρ constant. In both cases, the fixed parameter is set to the most recently obtained optimal solution.

The optimization of ρ is performed on the manifold of rank- r positive semi-definite matrices with unit trace, while ξ is constrained according to the measurement error model. The algorithm incorporates techniques from geometric optimization, such as tangent space projections. Let ρ_k, ξ_k be the values after step k of the algorithm

a. ρ step. The iteration starts by computing the Euclidean outer gradient $G_\xi = \mathcal{A}_{\xi_k}^\dagger(\hat{y} - \mathcal{A}(\rho_k, \xi_k))$, where $\mathcal{A}_\xi(\rho) = \mathcal{A}(\rho, \xi)$ denotes the linear map acting on ρ , of the least-squared deviation (3). The algorithm projects this gradient onto the tangent space of the manifold of rank- r matrices. This projection ensures that updates remain consistent with the manifold structure while accelerating convergence. The tangent space projection at a point ρ is computed as follows: Let $\rho = U\Lambda U^\dagger$ be the eigenvalue decomposition of ρ , where Λ is diagonal and the eigenvalues are arranged in decreasing order. Let $U^{(r)}$ denote the matrix containing the first r eigenvectors of U . The projection of the gradient is $P_{\mathcal{T}}(G) = G - (\mathbb{I} - P_U)G(\mathbb{I} - P_U)$, where $P_U = U^{(r)}(U^{(r)})^\dagger$.

The algorithm calculates the step width $\mu_k = \|P_{\mathcal{T}}(G)\|_F^2 / \|\mathcal{A}(\xi_k, P_{\mathcal{T}}(G))\|_F^2$ and updates the state $\rho' = \rho_k + \mu_k P_{\mathcal{T}}(\mathcal{A}_{\xi_k}^\dagger(\hat{y} - \mathcal{A}_{\xi_k}(\rho_k)))$. The result of the gradient step is then projected onto the set of rank- r positive semi-definite (PSD) matrices. The fixed-rank PSD projection is implemented as follows:

1. Project onto the set of Hermitian matrices as $\rho'' = (\rho' + \rho'^\dagger)/2$. Let $\rho'' = U\Lambda U^\dagger$ be the eigenvalue decomposition of ρ'' with unitary U and diagonal Λ .
2. Project onto the set of rank- r PSD matrices as $\rho^{(r)} = U\Lambda^{(r)}U^\dagger$, where $\Lambda^{(r)}$ contains only the r largest non-negative entries of Λ .

b. Normalization of ρ . After the projection step 2, $\rho^{(r)}$ remains an unnormalized PSD matrix. We observe that there is a multiplicative gauge freedom between ξ and ρ , i.e., the objective function (3) is invariant under the gauge transformation

$$(\xi, \rho) \mapsto (\xi/c, c\rho) \quad (\text{A1})$$

for any scalar c . We fix this gauge by setting $\rho_{k+1} = \rho^{(r)} / \text{tr}[\rho^{(r)}]$, and updating $\xi \mapsto \xi_{k+\frac{1}{2}} = \text{tr}[\rho^{(r)}]\xi_k$. In blind calibration we additionally allow for a global sign flip when

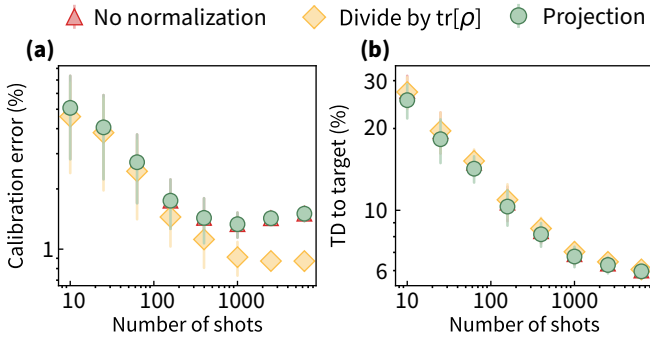


FIG. 5. **Comparison of normalization methods.** Using simulated data (1000 shots per basis) from a noisy three-qubit GHZ state with 1% Pauli noise added to each gate and miscalibration using the nine calibration parameters ξ_{actual} (C13), we perform blind calibration using three different state-normalization techniques: No normalization (triangles), dividing by the trace of the state (diamonds), and projection (circles). The resulting calibration error is shown in (a). Using these parameters, we perform calibrated state tomography, again comparing the aforementioned normalization methods. The trace distances to the target state are shown in (b). Shifting the trace of ρ into ξ performs better for blind calibration, while the projection (A2) performs better for calibrated state tomography.

projecting onto rank- r PSD matrices, since that sign can be absorbed in ξ .

We note that in step 2, one could alternatively directly project onto the set of (trace-normalized) quantum states by finding the number $\lambda \in \mathbb{R}$ that satisfies

$$\text{tr}[[\Lambda - \lambda]^{+,r}] = 1, \quad (\text{A2})$$

where $[a]^{+,r}$ denotes the entrywise projection of a tensor a onto its r largest nonnegative entries [32, 33]. This can be achieved, for instance, via a water-filling algorithm [32]. However, this projection alters the objective function and does not exploit the gauge freedom (A1). Indeed, we find, that our method of ‘shifting’ the trace of $\rho^{(r)}$ into ξ , performs better for blind calibration, see Fig. 5. However, the projection (A2) is used when we perform calibrated state tomography with a fixed calibration vector ξ , see Appendix B.

c. ξ step. For the optimization of ξ , we have the gradient $G_\rho = \mathcal{A}_\rho^\dagger(\hat{y} - \mathcal{A}_\rho(\xi))$ with $\mathcal{A}_\rho(\xi) = \mathcal{A}(\rho, \xi)$. The step width ν_k for ξ_k is determined using the same formula as above, omitting a tangent space projection. The updated vector $\xi' = \xi_{k+\frac{1}{2}} + \nu_k \mathcal{A}_{\rho_{k+1}}^\dagger(\hat{y} - \mathcal{A}_{\rho_{k+1}}(\xi_{k+\frac{1}{2}}))$ is then projected onto the set of valid calibration parameters via the projection \mathcal{P}_C yielding $\xi_{k+1} = \mathcal{P}_C(\xi')$.

d. *Termination criteria* The algorithm continues until the relative deviation of the objective function satisfies $\|\hat{y} - \mathcal{A}(\xi, \rho)\|_2 / \|\hat{y}\|_2 \leq \varepsilon$, where ε is a predefined threshold, or until a maximum of iterations is reached. Here we have used $\varepsilon = 10^{-2}$ and 100 maximum iterations.

e. *Initialization* When performing blind calibration, we initialize ρ and ξ by randomly sampling from a specified region around the anticipated values. For ξ , we have chosen a region within 15% of the directly measured values, while for ρ , we have chosen a region within 10% of the target state.

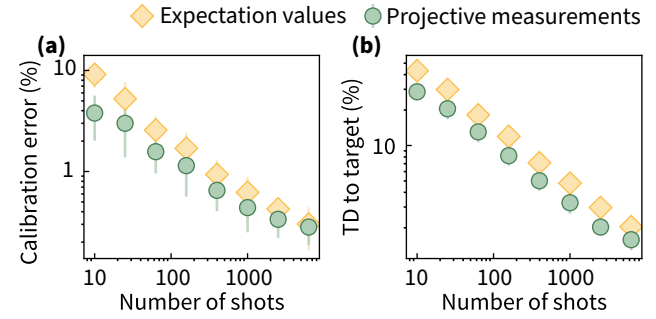


FIG. 6. **Comparison of projective measurement and expectation value calibrations.** Using simulated data (1000 shots per basis) from a noiseless three-qubit GHZ state and the nine calibration parameters ξ_{actual} (C13), we perform blind calibration using projective measurements (circles) and expectation value measurements (diamonds). The calibration error is shown in (a). The recovered parameters are then used to perform calibrated state tomography, for which the TD to the target state is shown in (b).

f. Expectation values versus projective measurements
In blind calibration, we use projective measurement data, compared to expectation values as elaborated in Ref. [23]. In the finite-sample regime, this more fine-grained data yields better recoveries of both the calibration parameters and the quantum state preparations, as demonstrated in Fig. 6. We observe that both for the calibration error and the TD to the target state, the projective measurements outperform the expectation value measurements, until a saturation point is reached where they reach equal performance.

Appendix B: Calibrated state tomography

In order to assess the quality and compare different calibrations, we use those calibrations to obtain tomographic state estimates from the same type of measurement data (projective Pauli measurements) on different states. To do this, we perform what we call ‘calibrated tomography’. In calibrated tomography, we fix a calibration ξ in our measurement model (2) and run Riemannian gradient descent on the set of quantum states in order to obtain the least-square fit (the minimizer of Eq. (3)) for ρ . Specifically, we run the same algorithm as in blind calibration, outlined in Appendix A, but rather than alternating the gradient steps, we fix the calibration ξ . At the end of the algorithm, we project onto the set of quantum states using the projection (A2) [33].

Importantly, while in blind calibration we want to exploit all available structural assumption in order to obtain the best possible calibration and therefore restrict to rank-1, when assessing a calibration, we want to obtain the most accurate state estimate, and thus remove the rank constraint, setting $r = D$ to be the Hilbert-space dimension D .

In our comparisons, we perform calibrated tomography using the ideal calibration ($\xi = (1, 0, \dots)$), corresponding to *standard tomography*, the directly measured estimate, and the blind calibration estimate.

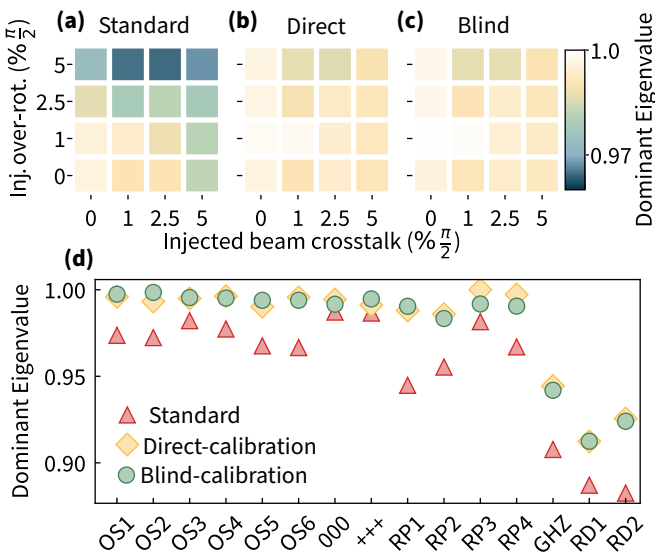


FIG. 7. **Dominant eigenvalues of calibrated state recoveries from experimental data.** States are recovered using full-rank standard, direct-calibration, and blind-calibration tomography for data with injected errors (a) and native errors (b). The dominant eigenvalues are close to 1, showing that the the states are near-pure, and justifying the rank-1 constraint in blind-calibration.

In Fig. 7, we show that the rank-1 constraint imposed in blind calibration is approximately true for the experimental data by comparing the dominant eigenvalue of the state estimate using calibrated tomography with different calibration parameter estimates. It becomes apparent that miscalibrations lead to a higher weight on subdominant principal components of the quantum state while the direct and blind calibrations have significantly larger dominant eigenvalues that are—as expected—close to 1 for product states, and somewhat smaller for states prepared by circuits involving 2-qubit gates.

The quality of different calibration can be measured in the trace distance of the calibrated-tomography estimate to the true state preparation. But while in simulations we can compute this quantity since the true (simulated) state preparation is known, this information is not available in experiments. This raises the question what a good measure of quality for the different calibrations is. Here, we use the trace distance (TD) to the target state, that is, the intended state preparation as a substitute for the trace distance to the true experimental state preparation. The intuition behind this choice is that a lower TD to the target state indicates a better calibration, since errors in the calibration estimate would have to conspire with the noise in the state preparation in order to yield a lower value compared to a more accurate calibration estimate. This expectation is confirmed in simulations of noisy state preparations. In Fig. 8, we show both the TD to the target state and to the noisy prepared state from which the data was generated as we scale the calibration from the ideal calibration $\xi_0 = (1, 0, \dots)$ to the actual calibration of the data set ξ_{actual} and beyond. As expected, the TD to the target state attains a minimum value at the actual calibration parameters, and gen-

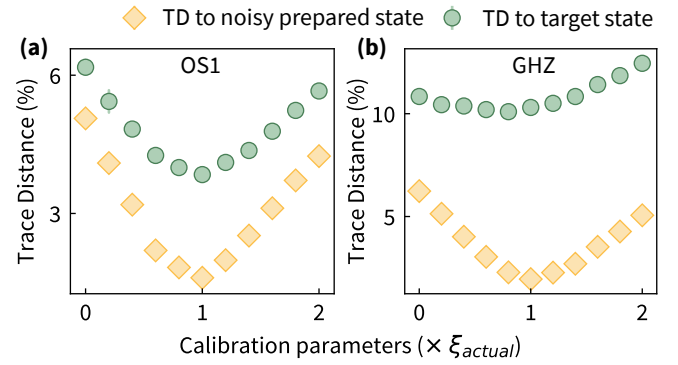


FIG. 8. **Evidence for validity of trace distance to the target state.** Comparison of the state estimate obtained from calibrated tomography with calibration parameters $(1 - c)\xi_{\text{ideal}} + c\xi_{\text{actual}}$ for $c \in [0, 2]$ with $\xi_{\text{ideal}} = (1, 0, \dots)$ and ξ_{actual} given in Eq. (C13) using 1000 simulated shots per measurement basis from from noisy state preparations using a Pauli noise channel with strength 1% per gate for the probe state OS1 (a) and the GHZ state (b). Shown are the TD to the noisy (simulated) state preparation (diamonds) and the target state (circles). Error bars are one standard deviation.

erally correlates with the trace distance to the true state preparation. We also find that the amount of correlation differs for different states. For example, for the GHZ state there seems to be a weaker correlation than for one of our probe states.

Appendix C: Error models

a. Over-rotations The transformed Pauli bases resulting from an over-rotation can be derived through transforming the Z basis by an over-rotated gate unitary. For the X basis, we rotate by $R_y\left(-\frac{\pi}{2} - \xi_{\text{OR}}\frac{\pi}{2}\right)$, where $\xi_{\text{OR}}\frac{\pi}{2}$ is assumed to be a small over-rotation angle. This yields

$$X \mapsto R_y\left(\frac{\pi}{2} + \xi_{\text{OR}}\frac{\pi}{2}\right) Z R_y\left(-\frac{\pi}{2} - \xi_{\text{OR}}\frac{\pi}{2}\right) \quad (\text{C1})$$

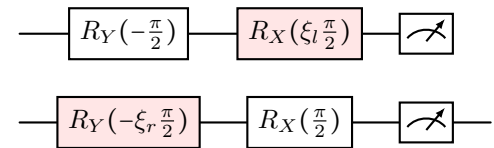
$$= \cos(\xi_{\text{OR}}\pi)X - \sin(\xi_{\text{OR}}\pi)Z. \quad (\text{C2})$$

Assuming the extra angle $\xi_{\text{OR}}\frac{\pi}{2}$ is small, we therefore obtain

$$X \mapsto X - \xi_{\text{OR}}Z \quad (\text{C3})$$

The same derivation applies for the Y basis.

b. Beam Crosstalk Transformations are determined by applying a modified gate unitary to the Z basis. For two qubits, the gates consist of the target qubit rotation and the crosstalk “gate” on the neighboring qubit(s). For example, ignoring any phase difference between target and neighbor, measuring in the XY basis results in the crosstalk circuit



for which we can construct the unitary,

$$U_{bc} = R_y^{(1)} \left(-\frac{\pi}{2} \right) R_y^{(2)} \left(-\xi_r \frac{\pi}{2} \right) R_x^{(1)} \left(\xi_l \frac{\pi}{2} \right) R_x^{(2)} \left(\frac{\pi}{2} \right). \quad (C4)$$

We can apply this unitary transformation to the Z basis as

$$Z \mapsto U_{bc} Z U_{bc}^\dagger \quad (C5)$$

and extract the Pauli terms which are first order in ξ , resulting in the transformation,

$$XY \mapsto XY + \xi_l \frac{\pi}{2} YY. \quad (C6)$$

Now, including the phase difference between the neighbor and target requires the use of arbitrary rotations, rather than strictly R_X and R_Y gates on the neighbors. The rotations applied to the left and right neighbors have a phase equal to that of the target phase plus ϕ_l or ϕ_r .

c. Bright and dark errors Unlike rotation errors, it is intuitive to model readout errors as a map Λ , acting on the projective measurements. For dark and bright errors, we can directly write the complete map:

$$|0\rangle\langle 0|_M \mapsto (1 - p_0) |0\rangle\langle 0| + p_0 |1\rangle\langle 1| \quad (C7)$$

$$|1\rangle\langle 1|_M \mapsto p_1 |0\rangle\langle 0| + (1 - p_1) |1\rangle\langle 1| \quad (C8)$$

d. PMT Spillover PMT spillover is not present in the single-ion case, so the simplest map Λ for PMT spillover is the two-ion case:

$$|00\rangle\langle 00|_M \mapsto |00\rangle\langle 00|_M \quad (C9)$$

$$|01\rangle\langle 01|_M \mapsto (1 - p_{\text{left}}) |01\rangle\langle 01|_M + p_{\text{left}} |11\rangle\langle 11|_M \quad (C10)$$

$$|10\rangle\langle 10|_M \mapsto (1 - p_{\text{right}}) |10\rangle\langle 10|_M + p_{\text{right}} |11\rangle\langle 11|_M \quad (C11)$$

$$|11\rangle\langle 11|_M \mapsto |11\rangle\langle 11|_M \quad (C12)$$

e. Parameter values for numerical benchmarks In our numerical benchmarks we fix the values of the calibration parameters to ξ_{actual} with components

$$\begin{aligned} \xi_{\text{OR}} &= 1\% \\ p_0 &= 0.32\% \\ p_1 &= 1.541\% \\ p_{\text{left}} &= 0.17\% \\ p_{\text{right}} &= 0.41\% \\ \xi_l &= 2.56\% \\ \xi_r &= 1.18\% \\ \phi_l &= \frac{\pi}{4} \\ \phi_r &= \frac{\pi}{8} \end{aligned} \quad (C13)$$

Appendix D: Native system calibration

1. Direct measurements

a. SPAM

We independently measure the state preparation and measurement (SPAM) errors in our system. We construct a SPAM matrix, which we can invert and apply to the measured populations to infer the SPAM-free results. Through this method, we also directly measure the dark and bright errors and the detector spillover in the system.

To construct this SPAM matrix, we use a single ion and adjust the trap voltages to move the ion into the locations the three ions occupy when trapped together. We prepare the ion either in the dark or in the bright state, the latter with a high-fidelity microwave pulse, before performing a state measurement. For each ion position, we measure the probability of a bright ion on each of the three detector channels. The probability of measuring the ion as bright at its position gives us the bright error, while the probability of measuring a bright ion at the unoccupied positions gives us the detector spillover. Similarly, we prepare the ion in its dark state to characterize the dark error.

From this information, we can reconstruct the probability of measuring any state for any prepared state without Raman addressing error, giving us a complete readout matrix, which we use to correct the data.

b. Beam crosstalk

To measure the beam crosstalk present in the system, we prepare a chain of three ions in the state $|000\rangle$. We apply a single individual target beam and measure the resulting Rabi flop on each qubit, including the target. We calculate the ratio between the target Rabi frequency and the neighboring Rabi frequencies for each ion pair, giving us the magnitude of beam crosstalk. We find that the nearest-neighbor crosstalk magnitudes are asymmetric in direction, but consistent across ion positions.

2. Blind calibration

a. Optimal states

We observe that some states do not provide accurate calibrations for particular error types. We predict that this behavior results from the state's lack of sensitivity to the error. We predict two cases in which the probe state may give bad results.

1. The measurement data for the state is insensitive to certain measurement errors. In this case, the ideal measurement, $\mathcal{A}_0(\rho)$ is approximately equal to the calibrated model, $\mathcal{A}(\xi, \rho)$.

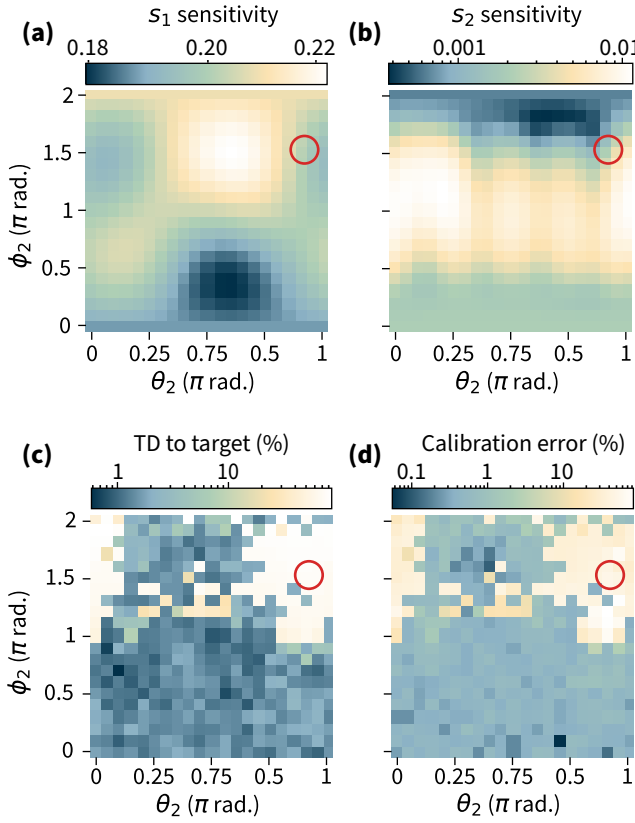


FIG. 9. **State sensitivity tests** for a noiseless three-qubit random product state, RP1, simulated with miscalibrations ξ_{actual} (C13). The two outer qubits are held at fixed angles, while the middle qubit is scanned through all possible states. The trace distance to the target and the calibration error presents complex features. The product state is shown by the red circle, and is seen to be particularly poor.

2. The measurement data are sensitive to the measurement error, but the optimal solution to the uncalibrated recovery is still a valid quantum state, that is, $\mathcal{A}^{-1}(y) \in \mathcal{D}(r)$. In this case, the density matrix constraint is not sufficient to distinguish a measurement error from a state-preparation error, resulting in a plateau in the optimization landscape.

We propose two methods for calculating these sensitivities:

1. $s_1(\xi, \rho) \doteq \|\mathcal{A}(\xi, \rho) - \mathcal{A}_0(\rho)\|$
2. $s_2(\xi, \rho) \doteq \|\mathcal{A}_0^{-1}(\mathcal{A}(\xi, \rho)) - \mathcal{P}_{\mathcal{D}(r)}[\mathcal{A}_0^{-1}(\mathcal{A}(\xi, \rho))]\|$

We test whether these proposed sensitivity measurements can predict the performance of the blind calibration by simulating three-qubit product state recoveries and sensitivities. We vary the angle of the center qubit over the Bloch sphere, measuring s_1 and s_2 and performing a blind calibration for each unique state. We find that the proposed sensitivity measurements s_1 and s_2 are not correlated to the performance of the blind calibration as shown in Fig. 9.

Therefore, in order to find an optimal set of states, we look only to the performance of the blind calibration. We optimize over three-qubit product states defined by (θ_i, ϕ_i) , for

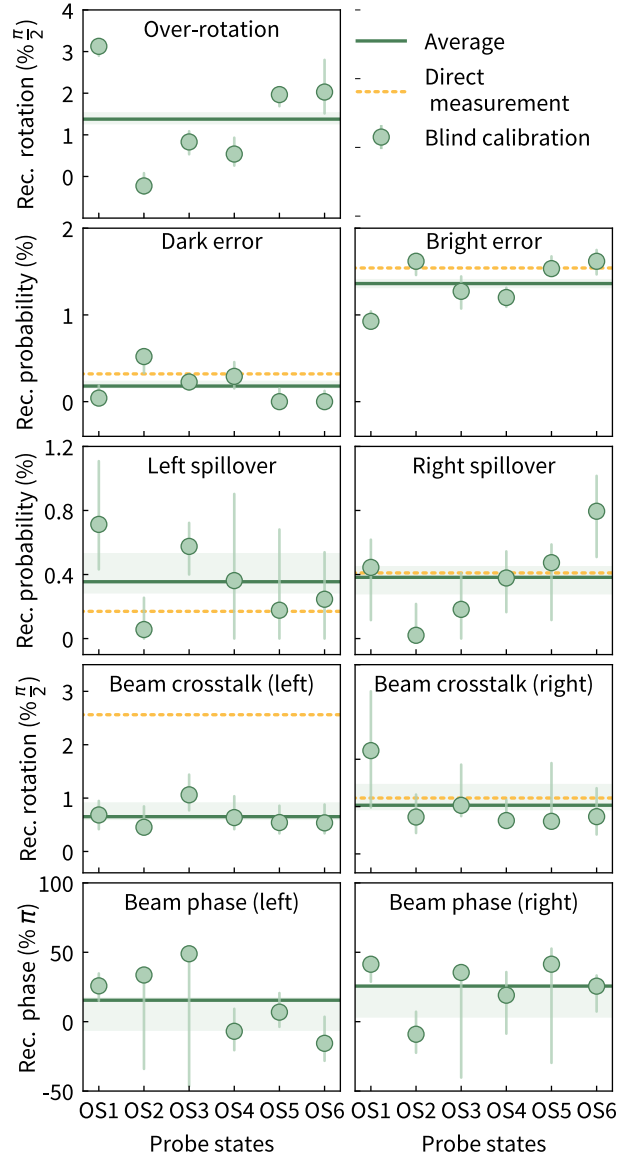


FIG. 10. **Complete set of native calibration parameters** of the experimental system recovered using blind calibration and direct calibration. The recovered values for each state (circles) and their averages (solid line) are compared to the direct experimental measurement (dashed line) where available.

each i qubit. For each state, we compute an objective which takes into account the calibration error at each value over the range of expected ξ . First, we minimize the average calibration error over the range. Second, we minimize the maximum total calibration error. We perform this optimization with and without measurement shot noise, and with a normalized and non-normalized calibration error measurement. This results in six optimal probe states defined by the azimuthal and polar angles as $(\theta_1, \phi_1, \theta_2, \phi_2, \theta_3, \phi_3)$ in units π radians:

1. **OS1** with angles (0.910, 1.978, 0.475, 0.378, 0.467, 0.480)
2. **OS2** with angles (0.463, 0.846, 0.742, 1.618, 0.530,

0.726)

3. **OS3** with angles (0.0316, 0.259, 0.374, 1.820, 0.372, 0.795)
4. **OS4** with angles (0.993, 1.954, 0.494, 0.999, 0.0767, 1.521)
5. **OS5** with angles (0.870, 1.967, 0.406, 1.012, 0.426, 0.548)
6. **OS6** with angles (0.352, 1.380, 0.707, 0.243, 0.448, 0.219)

b. *Test states*

We use nine states to test the blind calibration. For product states, we define the azimuthal and polar angles for each qubit as: $(\theta_1, \phi_1, \theta_2, \phi_2, \theta_3, \phi_3)$ in units π radians. The test product states are

1. $|000\rangle$ with angles (0, 0, 0, 0, 0, 0)
2. $|+++ \rangle$ with angles (0.5, 0, 0.5, 0, 0.5, 0)
3. **RP1** with angles (0.871, 1.427, 0.713, 1.190, 0.693, 1.477)
4. **RP2** with angles (0.723, 1.198, 0.924, 1.533, 0.871, 0.485)
5. **RP3** with angles (0.736, 0.559, 0.654, 0.422, 0.783, 1.211)

6. **RP4** with angles (0.957, 0.105, 0.942, 0.270, 0.704, 0.773)

We also test three entangled states. Entanglement is generated using a variant [34] of the Molmer-Sorensen (MS) gates [35], parameterized by the angle χ_{ij} on qubits i and j , where $\chi_{ij} = \frac{\pi}{4}$ produces a fully-entangled state.

1. **GHZ**, the Greenberger-Horne-Zeilinger state $|000\rangle + |111\rangle$.
2. **RD1** with single-qubit rotations by angles (0.872, 0.426, 0.714, 0.190, 0.693, 0.477), then fully entangling MS gates on each qubit pair.
3. **RD2** with single-qubit rotations by angles (0.722, 0.198, 0.923, 1.533, 0.871, 0.485), then fully entangling MS gates on each qubit pair.

3. Full recovery

We compare all measurements (direct and blind) of the native calibration parameters in Fig. 10. We find good agreement between the parameters obtained in blind calibration and the directly measured values where available. An exception is the left beam crosstalk parameter ξ_l , where the directly measured value is inconsistent with the blind calibration estimates, which are consistent across the different probe states.

[1] Z. Hradil, *Quantum-State Estimation*, Phys. Rev. A **55**, R1561 (1997).

[2] D. F. V. James, P. G. Kwiat, W. J. Munro, and A. G. White, *Measurement of Qubits*, Phys. Rev. A **64**, 052312 (2001).

[3] A. Luis and L. L. Sánchez-Soto, *Complete Characterization of Arbitrary Quantum Measurement Processes*, Phys. Rev. Lett. **83**, 3573 (1999).

[4] J. S. Lundeen, A. Feito, H. Coldenstrodt-Ronge, K. L. Pregnell, C. Silberhorn, T. C. Ralph, J. Eisert, M. B. Plenio, and I. A. Walmsley, *Tomography of Quantum Detectors*, Nature Phys **5**, 27 (2009).

[5] I. L. Chuang and M. A. Nielsen, *Prescription for Experimental Determination of the Dynamics of a Quantum Black Box*, Journal of Modern Optics **44**, 2455 (1997), arXiv:quant-ph/9610001.

[6] J. F. Poyatos, J. I. Cirac, and P. Zoller, *Complete Characterization of a Quantum Process: The Two-Bit Quantum Gate*, Phys. Rev. Lett. **78**, 390 (1997).

[7] G. M. D'Ariano, L. Maccone, and P. L. Presti, *Quantum Calibration of Measurement Instrumentation*, Phys. Rev. Lett. **93**, 250407 (2004).

[8] L. Motka, B. Stoklasa, J. Rehacek, Z. Hradil, V. Karasek, D. Mogilevtsev, G. Harder, C. Silberhorn, and L. L. Sánchez-Soto, *Efficient Algorithm for Optimizing Data-Pattern Tomography*, Phys. Rev. A **89**, 054102 (2014).

[9] J. Řeháček, D. Mogilevtsev, and Z. Hradil, *Operational Tomography: Fitting of Data Patterns*, Phys. Rev. Lett. **105**, 010402 (2010).

[10] R. Schmidt, *Multiple Emitter Location and Signal Parameter Estimation*, IEEE Transactions on Antennas and Propagation **34**, 276 (1986).

[11] R. Roy, A. Paulraj, and T. Kailath, *Estimation of Signal Parameters via Rotational Invariance Techniques - ESPRIT*, in *MILCOM 1986 - IEEE Military Communications Conference: Communications-Computers: Teamed for the 90's*, Vol. 3 (1986) pp. 41.6.1–41.6.5.

[12] S. T. Merkel, J. M. Gambetta, J. A. Smolin, S. Poletto, A. D. Córcoles, B. R. Johnson, C. A. Ryan, and M. Steffen, *Self-Consistent Quantum Process Tomography*, Phys. Rev. A **87**, 062119 (2013).

[13] R. Blume-Kohout, J. K. Gamble, E. Nielsen, J. Mizrahi, J. D. Sterk, and P. Maunz, *Robust, Self-Consistent, Closed-Form Tomography of Quantum Logic Gates on a Trapped Ion Qubit*, (2013), arXiv:1310.4492.

[14] R. Blume-Kohout, J. K. Gamble, E. Nielsen, K. Rudinger, J. Mizrahi, K. Fortier, and P. Maunz, *Demonstration of Qubit Operations below a Rigorous Fault Tolerance Threshold with Gate Set Tomography*, Nature Communications **8**, 14485 (2017).

[15] R. Brieger, I. Roth, and M. Kliesch, *Compressive Gate Set Tomography*, *PRX Quantum* **4**, 010325 (2023), [arXiv:2112.05176](https://arxiv.org/abs/2112.05176).

[16] D. Mogilevtsev, J. Řeháček, and Z. Hradil, *Relative Tomography of an Unknown Quantum State*, *Phys. Rev. A* **79**, 020101 (2009).

[17] D. Mogilevtsev, *Calibration of Single-Photon Detectors Using Quantum Statistics*, *Phys. Rev. A* **82**, 021807 (2010).

[18] D. Mogilevtsev, J. Řeháček, and Z. Hradil, *Self-Calibration for Self-Consistent Tomography*, *New J. Phys.* **14**, 095001 (2012).

[19] J. Y. Sim, J. Shang, H. K. Ng, and B.-G. Englert, *Proper Error Bars for Self-Calibrating Quantum Tomography*, (2019), [arXiv:1904.11202](https://arxiv.org/abs/1904.11202).

[20] A. M. Brańczyk, D. H. Mahler, L. A. Rozema, A. Darabi, A. M. Steinberg, and D. F. V. James, *Self-Calibrating Quantum State Tomography*, *New J. Phys.* **14**, 085003 (2012).

[21] I. D. Moore and S. J. van Enk, *Self-Consistent Tomography and Measurement-Device Independent Cryptography*, (2020), [arXiv:2006.06559](https://arxiv.org/abs/2006.06559).

[22] A. Jayakumar, S. Chessa, C. Coffrin, A. Y. Lokhov, M. Vuffray, and S. Misra, *Universal Framework for Simultaneous Tomography of Quantum States and SPAM Noise*, *Quantum* **8**, 1426 (2024), [arXiv:2308.15648](https://arxiv.org/abs/2308.15648).

[23] I. Roth, J. Wilkens, D. Hangleiter, and J. Eisert, *Semi-Device-Dependent Blind Quantum Tomography*, *Quantum* **7**, 1053 (2023).

[24] R. Stárek, M. Bielak, and M. Ježek, *Measurement-Device Agnostic Quantum Tomography*, (2024), [arXiv:2407.13011](https://arxiv.org/abs/2407.13011).

[25] M. Ma and J. Shang, *Corrupted Sensing Quantum State Tomography*, (2024), [arXiv:2405.14396](https://arxiv.org/abs/2405.14396).

[26] R. Stricker, D. Vodola, A. Erhard, L. Postler, M. Meth, M. Ringbauer, P. Schindler, R. Blatt, M. Müller, and T. Monz, *Characterizing Quantum Instruments: From Non-Demolition Measurements to Quantum Error Correction*, *PRX Quantum* **3**, 030318 (2022), [arXiv:2110.06954](https://arxiv.org/abs/2110.06954).

[27] S. Olmschenk, K. C. Younge, D. L. Moehring, D. N. Matsukevich, P. Maunz, and C. Monroe, *Manipulation and Detection of a Trapped Yb^+ Hyperfine Qubit*, *Phys. Rev. A* **76**, 052314 (2007).

[28] S. Debnath, N. M. Linke, C. Figgatt, K. A. Landsman, K. Wright, and C. Monroe, *Demonstration of a Small Programmable Quantum Computer with Atomic Qubits*, *Nature* **536**, 63 (2016).

[29] H.-Y. Huang, R. Kueng, and J. Preskill, *Predicting Many Properties of a Quantum System from Very Few Measurements*, *Nature Physics* **16**, 1050 (2020).

[30] J. Helsen, M. Ioannou, J. Kitzinger, E. Onorati, A. H. Werner, J. Eisert, and I. Roth, *Estimating Gate-Set Properties from Random Sequences*, (2022), [arXiv:2110.13178](https://arxiv.org/abs/2110.13178).

[31] A. Elben, S. T. Flammia, H.-Y. Huang, R. Kueng, J. Preskill, B. Vermersch, and P. Zoller, *The Randomized Measurement Toolbox*, *Nat Rev Phys* **5**, 9 (2023), [arXiv:2203.11374](https://arxiv.org/abs/2203.11374).

[32] J. A. Smolin, J. M. Gambetta, and G. Smith, *Efficient Method for Computing the Maximum-Likelihood Quantum State from Measurements with Additive Gaussian Noise*, *Phys. Rev. Lett.* **108**, 070502 (2012).

[33] M. Guță, J. Kahn, R. Kueng, and J. A. Tropp, *Fast State Tomography with Optimal Error Bounds*, *J. Phys. A: Math. Theor.* **53**, 204001 (2020), [arXiv:1809.11162](https://arxiv.org/abs/1809.11162).

[34] T. Choi, S. Debnath, T. A. Manning, C. Figgatt, Z.-X. Gong, L.-M. Duan, and C. Monroe, *Optimal Quantum Control of Multi-mode Couplings between Trapped Ion Qubits for Scalable Entanglement*, *Phys. Rev. Lett.* **112**, 190502 (2014).

[35] A. Sørensen and K. Mølmer, *Quantum Computation with Ions in Thermal Motion*, *Phys. Rev. Lett.* **82**, 1971 (1999).